

An internal streaming instability in regenerators

J. H. So, G. W. Swift, and S. Backhaus*

Condensed Matter and Thermal Physics Group

Los Alamos National Laboratory

Los Alamos, New Mexico 87545

(Dated: April 24, 2006)

Abstract

Various oscillating-wave thermodynamic devices, including orifice and feedback pulse tube refrigerators, thermoacoustic-Stirling hybrid engines, cascaded thermoacoustic engines, and traditional Stirling engines and refrigerators, utilize regenerators to amplify acoustic power (engines) or to pump heat acoustically up a temperature gradient (refrigerators). As such a regenerator is scaled to higher power or operated at lower temperatures, the thermal and hydrodynamic communication transverse to the acoustic axis decreases, allowing for the possibility of an internal acoustic streaming instability with regions of counterflowing streaming that carry significant heat leak down the temperature gradient. The instability is driven by the nonlinear flow resistance of the regenerator, which results in different hydrodynamic flow resistances encountered by the oscillating flow and the streaming flow. The instability is inhibited by several other mechanisms, including acoustically transported enthalpy flux and axial and transverse thermal conduction in the regenerator solid matrix. A calculation of the stability limit caused by these effects reveals that engines are immune to a streaming instability while, under some conditions, refrigerators can exhibit an instability. The calculation is compared to experimental data obtained with a specially built orifice pulse tube refrigerator whose regenerator contains many thermocouples to detect a departure from transverse temperature uniformity.

PACS numbers: 43.25.Nm 43.35.Ud

I. INTRODUCTION

The regenerator¹ is a critical component of many oscillating-wave thermodynamic devices including orifice² and feedback³ pulse tube refrigerators, thermoacoustic-Stirling hybrid engines,⁴⁻⁶ cascade thermoacoustic engines,⁷ and traditional Stirling engines and refrigerators.⁸ In combination with the temperature gradient, the regenerator amplifies acoustic power in engines and it allows the acoustic wave to pump heat in refrigerators.

To analyze regenerators, researchers have generally assumed one-dimension behavior, i.e., that everything is independent of transverse coordinates y and z but depends only on the axial position x . However, awareness is growing that non-trivial multi-dimensional behavior and an associated penalty in performance can occur in the regenerators of pulse-tube and Stirling cryocoolers. Such multi-dimensional behavior has been described for transverse variation in the hydraulic radius of regenerators⁹ and for three identical regenerators operated in parallel.¹⁰

Most regenerators are made of stacked screen or other tortuous porous media whose nonlinear flow resistance generates a complicated interaction between the oscillating and steady flows. The result is that the oscillating and steady flows encounter different flow resistances which depend on temperature in different ways. A small spatial perturbation in the mean temperature transverse to the acoustic axis leads to different flow resistances for the oscillating and streaming flows in different regions of the regenerator, resulting in a small circulating streaming flow, as illustrated in Fig. 1. Whether the streaming flow acts to amplify or suppress the original perturbation depends on many variables, including the direction of the streaming flow and the temperatures of the heat exchangers at the two ends of the regenerator. The original perturbation might be amplified by this effect if $T_w < T_a$ and suppressed if $T_w > T_a$ where T_a is ambient temperature and T_w is the working temperature (i.e., the hot temperature for an engine and the cold temperature for a refrigerator). Even if the resulting streaming acts to amplify the original perturbation, other effects, such as thermal conduction or acoustic enthalpy transport, will attempt to suppress it.

As such an engine or refrigerator is scaled to higher power, the cross-sectional area of its regenerator must increase proportionally to keep its design near a thermodynamic optimum, but its length remains approximately constant. At some point, the transverse thermal and hydrodynamic communication within the regenerator becomes so weak that it cannot

counteract the streaming caused by a transverse mean-temperature perturbation, and an instability may arise. Whether or not this occurs depends on the balance among all these effects. If an instability does occur, the streaming flow carries additional energy flux down the temperature gradient, resulting in reduced efficiency in the engine or refrigerator.

Using a linear stability analysis, we add to a streaming-free solution a perturbation that grows or decays exponentially in time. By comparing different terms that either drive or inhibit the instability, we show when the combination of these mechanisms results in instability, i.e. an exponentially growing perturbation. The instability is experimentally investigated using a specially designed and heavily instrumented orifice pulse tube refrigerator. Thermocouples placed inside the refrigerator's regenerator detect the presence of streaming through measurements of the mean temperature distribution. When the acoustic power flux is high and the total energy flux and cold-end temperature are low, a mean temperature variation about the axial midplane of the regenerator is detected, indicating the presence of a streaming instability. The values of the acoustic power flux, total energy flux, and cold-end temperature at the threshold of instability are found to be in only qualitative agreement with theory.

II. THEORY

To search for an internal streaming instability analytically, we will combine a thermoacoustic analysis¹¹ through second order in the acoustic amplitude with a linear perturbation analysis.¹² Carrying the thermoacoustic analysis to second order includes the lowest-order time-averaged energy and mass-flux effects, which can interact in the perturbation analysis to produce exponential growth of both. A similar approach was taken in an investigation of a related instability.¹³ First, a simplified model of the acoustics in the regenerator is used to establish relationships among streaming-free first-order variables. Then the important second-order streaming-free quantities—the time-averaged energy flux and the second-order velocity—are derived from the first-order quantities. Thus far, all variables depend on the axial coordinate in the regenerator but are independent of transverse coordinates. Then, a perturbation is added to the solution that depends on the transverse coordinates, and the analysis shows that it can either grow or decay exponentially with time, depending on the competition among a number of stabilizing and destabilizing effects. To make the

mathematics as simple as possible, we make a number of restrictive and potentially unrealistic assumptions. We neglect any time-phase difference between first-order pressure and first-order velocity throughout the regenerator. We assume that the velocity perturbation is nonzero only parallel to the acoustic axis. We neglect oscillations at any frequency but the fundamental. And we arbitrarily choose a mathematically simple functional form for the axial spatial dependence of the perturbation. We hope that some or all of these restrictive assumptions can be avoided in future work.

A. Streaming-free solution

Using a variation on the usual acoustic expansion and time-harmonic notation,¹¹ the streaming-free solution can be written

$$p(x, t) = p_m + p_{1R}(x) \cos \omega t - p_{1I}(x) \sin \omega t + p_{20}(x) + p_{22R}(x) \cos 2\omega t - p_{22I}(x) \sin 2\omega t + \dots \quad (1)$$

$$u(x, t) = u_{1R}(x) \cos \omega t - u_{1I}(x) \sin \omega t + u_{20}(x) + u_{22R}(x) \cos 2\omega t - u_{22I}(x) \sin 2\omega t + \dots, \quad (2)$$

$$T(x, t) = T_m(x) + T_{1R}(x) \cos \omega t - T_{1I}(x) \sin \omega t + T_{20}(x) + T_{22R}(x) \cos 2\omega t - T_{22I}(x) \sin 2\omega t + \dots \quad (3)$$

where p , u , and T are the working-gas pressure, x component of velocity, and temperature, respectively. Here and throughout this paper, variables with the subscript m , $1R$, $1I$, $22R$, $22I$, or 20 are real. The fundamental angular frequency of the oscillation is ω , t is time, and x is the coordinate along the axis of the regenerator, with $x = 0$ at the ambient face and $x = x_w$ at the working-temperature face. Variables describing the gas, such as $u_{1R}(x)$ and $T_{1R}(x)$, represent local spatial averages over small volumes of gas including many pores, not microscopic values needed to describe spatial dependencies within the tortuous geometry of a single pore. However, the time-averaged energy-flux density \dot{h} , which describes energy flux through both the gas and solid, is a local spatial average over a small volume of both gas and solid including many pores. Thus, if A is the regenerator's cross-sectional area and ϕ is its volume porosity, the total volume flow rate is $\phi A u$ and the total energy flux is $A \dot{h}_x$.

The representation in Eqs. (1) through (3) is equivalent to the usual complex notation

$$p(x, t) = p_m + \text{Re}[p_1(x)e^{i\omega t}] + p_{20}(x) + \text{Re}[p_{22}(x)e^{i2\omega t}] + \dots, \quad (4)$$

$$u(x, t) = \text{Re}[u_1(x)e^{i\omega t}] + u_{20}(x) + \text{Re}[u_{22}(x)e^{i2\omega t}] + \dots, \quad (5)$$

$$T(x, t) = T_m(x) + \text{Re}[T_1(x)e^{i\omega t}] + T_{20}(x) + \text{Re}[T_{22}(x)e^{i2\omega t}] + \dots, \quad (6)$$

with, *e.g.*, $p_1(x) = p_{1R}(x) + ip_{1I}(x)$ and with variables having subscript 1 or 22 being complex. At each step in the calculation, the choice of notation will be determined by convenience.

Using the notation in Eqs. (4)-(6), the continuity equation expanded to first order and averaged over the small scale is¹⁴

$$\frac{du_1}{dx} - \frac{1}{T_m} \frac{dT_m}{dx} u_1 = -\frac{i\omega\rho_1}{\rho_m}. \quad (7)$$

In effective regenerators, the excellent thermal contact between the working gas and the regenerator solid renders the density oscillations nearly isothermal, so that $\rho_1 = (\rho_m/p_m)p_1$. If the gas volume in the regenerator is small enough that its compressibility can be ignored, the ρ_1 term on the right-hand side (RHS) of Eq. (7) can be neglected, so that

$$u_1(x) = u_1(0) \frac{T_m(x)}{T_a}. \quad (8)$$

The subscripts a and w refer to mean variables evaluated at the ambient end $x = 0$ and the working end $x = x_w$ of the regenerator, respectively. Without loss of generality, the phase of $u_1(0)$ can be chosen so that

$$u_{1R}(x) = u_{1R}(0) \frac{T_m(x)}{T_a} > 0, \quad (9)$$

$$u_{1I}(x) = 0. \quad (10)$$

Under typical operating conditions, p_1 and u_1 at $x = 0$ are nearly in phase so that

$$p_{1R}(x) > 0, \quad (11)$$

$$p_{1I}(x) = 0. \quad (12)$$

In general, the second-order mass-flux density is given by

$$\dot{m}_{20} = \text{Re}[\rho_1 u_1^*]/2 + \rho_m u_{20} = \frac{\rho_m}{2p_m} p_{1R} u_{1R} + \rho_m u_{20}, \quad (13)$$

where the superscript $*$ stands for complex conjugation. We have again assumed that the density oscillations are nearly isothermal. In the streaming-free state $\dot{m}_{20} = 0$, and if the typically small variation in p_{1R} through the regenerator is ignored, u_{20} can be expressed

$$u_{20}(x) = -\frac{p_{1R} u_{1R}(x)}{2p_m} = u_{20}(0) \frac{T_m(x)}{T_a}. \quad (14)$$

showing that u_{1R} and u_{20} have approximately the same spatial dependence.

If the perimeter of the regenerator is well insulated, the time-averaged second-order energy-flux density $\dot{h}_{2,x}$ is independent of both x and t in the streaming-free steady state, indicating there is no buildup of energy inside the regenerator.¹¹ A perfect regenerator would have $\dot{h}_{2,x} = 0$, and in realistic regenerators $\dot{h}_{2,x}$ is small—much smaller than the acoustic intensity. The small T_1 that is neglected above in the analysis of $u_1(x)$ contributes significantly to this small energy-flux density and cannot be neglected in $\dot{h}_{2,x}$.

B. Perturbed solution

An exponentially growing or decaying perturbation is added to the streaming-free solution derived in the previous section, so that the complete solution is of the form

$$p(x, y, t) = p_m + p_{1R} \cos \omega t + p_{20}(x) + [\delta p_{1R}(x, y) \cos \omega t - \delta p_{1I}(x, y) \sin \omega t + \delta p_{20}(x, y)] e^{\epsilon t}, \quad (15)$$

$$u(x, y, t) = u_{1R}(x) \cos \omega t + u_{20}(x) + u_{22R}(x) \cos(2\omega t) - u_{22I}(x) \sin(2\omega t) + [\delta u_{1R}(x, y) \cos \omega t - \delta u_{1I}(x, y) \sin \omega t + \delta u_{20}(x, y) + \delta u_{22R}(x) \cos(2\omega t) - \delta u_{22I}(x) \sin(2\omega t)] e^{\epsilon t}, \quad (16)$$

$$T(x, y, t) = T_m(x) + \delta T_m(x, y) e^{\epsilon t} + T_{1R}(x, y) \cos \omega t - T_{1I}(x, y) \sin \omega t + [\delta T_{1R}(x, y) \cos \omega t - \delta T_{1I}(x, y) \sin \omega t] e^{\epsilon t}, \quad (17)$$

$$\rho(x, y, t) = \text{similar to } T, \quad (18)$$

$$\dot{h}_x(x, y, t) = \dot{h}_{2,x} + \delta \dot{h}_x(x, y) e^{\epsilon t}, \quad (19)$$

$$\dot{h}_y(x, y, t) = \delta \dot{h}_y(x, y) e^{\epsilon t}, \quad (20)$$

where we only allow variation in one of the coordinates transverse to the acoustic axis, *i.e.* y , and we have carried the expansions only as far as the terms that we will discuss later. In this calculation, we have in mind a regenerator with one long (y) and one short (z) transverse dimension such that variations in temperature due to a perturbation are more likely to take hold in the long dimension. The perturbation includes both oscillating and non-oscillating terms. The oscillating perturbations are assumed to have the same frequency as the corresponding terms in the streaming-free solution and amplitudes that change slowly, but exponentially, in time compared to the acoustic period, *i.e.* $|\epsilon| \ll \omega$. This two-time-scale approach allows the explicit separation of the slow change of the instability from the

rapid acoustic oscillations. Non-oscillating terms also change exponentially in time with the same time constant as the amplitudes of the oscillating terms. We assume $\delta\omega$ is zero. For a refrigerator this can be regarded as a simple consequence of how the system is driven, *e.g.* by a linear motor at fixed frequency. For a thermoacoustic-Stirling hybrid engine, cascaded thermoacoustic engine, or Stirling engine, one can similarly assume that the complex load impedance is deliberately varied to keep ω fixed.

Substituting the full solution of Eqs. (15)-(20) into the continuity equation, expanding to first order in the perturbation, taking $\delta\rho_1 = 0$ for the reasons described below Eq. (7), utilizing the results of Eq. (8), and recalling that we are neglecting transverse flow, we find

$$\frac{d\delta u_1}{dx} - \frac{1}{T_m} \frac{dT_m}{dx} \delta u_1 = \frac{u_1(0)}{T_a} \left[\frac{d\delta T_m}{dx} - \frac{\delta T_m}{T_m} \frac{dT_m}{dx} \right]. \quad (21)$$

The solution to this differential equation for δu_1 is given by

$$\delta u_1(x, y) = \delta u_1(0, y) \frac{T_m(x)}{T_a} + \frac{u_1(0)}{T_a} \delta T_m(x, y), \quad (22)$$

where the boundary condition $\delta T_m(0, y) = 0$ has been used. This boundary condition implies that the heat transfer provided by the heat exchanger at $x = 0$ is sufficient to hold the temperature perturbation at zero at the heat exchanger despite the streaming. (Later, we will use the same condition at $x = x_w$.)

Equation (22) can be broken up into real and imaginary parts

$$\delta u_{1R}(x, y) = \delta u_{1R}(0, y) \frac{T_m(x)}{T_a} + u_{1R}(0) \frac{\delta T_m(x, y)}{T_a}, \quad (23)$$

$$\delta u_{1I}(x, y) = \delta u_{1I}(0, y) \frac{T_m(x)}{T_a}. \quad (24)$$

To determine $\delta u_{1R}(0, y)$ and $\delta u_{1I}(0, y)$ in Eqs. (23) and (24), we must consider the first-order Navier-Stokes equation. The full solution given in Eqs. (15) through (17) is substituted into the spatially averaged Navier-Stokes equation for screens,¹⁴ and the result is expanded to first order in the perturbation for all terms (dropping terms that are obviously of zero order in the perturbation). Additionally, the linear term is expanded to acoustic first order, and the nonlinear term is expanded to acoustic second order. This intermediate result is

$$\begin{aligned} - \frac{\partial}{\partial x} [\delta p_{1R} \cos \omega t - \delta p_{1I} \sin \omega t] &= \frac{c_1}{8r_h^2} [\mu_m \delta u_{1R} \cos \omega t - \mu_m \delta u_{1I} \sin \omega t + \delta \mu_m u_{1R} \cos \omega t] \\ &+ \frac{c_2}{2r_h} \rho_m [u_{1R} \cos \omega t + \delta u_{1R} \cos \omega t - \delta u_{1I} \sin \omega t] [u_{1R} \cos \omega t + \delta u_{1R} \cos \omega t - \delta u_{1I} \sin \omega t] \\ &+ \frac{c_2}{2r_h} \delta \rho_m u_{1R}^2 \cos \omega t |\cos \omega t|, \end{aligned} \quad (25)$$

where c_1 and c_2 parameterize the regenerator flow resistance,¹⁴ r_h is the hydraulic radius,¹⁴ and μ is the gas viscosity. The presence of the absolute value sign in the nonlinear term complicates the expansion by forcing the temporary retention of certain terms that may appear to be of higher order than we later keep. To isolate δp_{1R} or δp_{1I} , Eq. (25) is multiplied by $(\cos \omega t)/\pi$ or $(\sin \omega t)/\pi$ and integrated with respect to ωt from 0 to 2π , being careful to split the integration into two at the zero crossings of the terms inside the absolute value signs. To lowest order in δu_{1I} , the result for δp_{1I} is

$$-\frac{\partial \delta p_{1I}}{\partial x} = \left[\frac{c_1 \mu_a}{8r_h^2} \left(\frac{T_m}{T_a} \right)^b + \frac{4c_2}{3\pi r_h} \rho_a u_{1R}(0) \right] \frac{T_m(x)}{T_a} \delta u_{1I}(0, y), \quad (26)$$

where b accounts for the temperature dependence of viscosity via $\mu(T) = \mu_a(T/T_a)^b$. Assuming that the spaces at the ends of the regenerator are open enough so that δp_{1I} and δp_{1R} cannot have any y dependence at $x = 0$ or x_w , i.e. $\delta p_{1I}(0, y) = \delta p_{1I}(x_w, y) = 0$, the integral of Eq. (26) from 0 to x_w must be zero. The terms inside of the square brackets are always positive, and therefore $\delta u_{1I}(0, y) = 0$ and $\delta u_{1I}(x, y) = 0$. This result, combined with the assumption that $\delta p_{1I}(0, y) = 0$ and Eq. (26), shows that $\delta p_{1I}(x, y) = 0$.

With the perturbation greatly simplified by the conclusion that $\delta u_{1I}(x, y) = 0$, δp_{1R} is isolated from Eq. (25) yielding

$$-\frac{8r_h^2}{c_1 \mu_a} \frac{\partial \delta p_{1R}}{\partial x} = \delta u_{1R}(0) \left[\left(\frac{T_m}{T_a} \right)^{1+b} + 2\Gamma \left(\frac{T_m}{T_a} \right) \right] + \frac{\delta T_m}{T_a} u_{1R}(0) \left[(1+b) \left(\frac{T_m}{T_a} \right)^b + \Gamma \right] \quad (27)$$

to lowest order in δu_{1R} , where $\Gamma = 8c_2 N_{R,a}/3\pi c_1$ and $N_{R,a}$ is the Reynolds number $N_R = 4\rho_m u_{1R} r_h / \mu_m$ evaluated at the ambient end of the regenerator. Next, Eq. (27) is integrated with respect to x from 0 to x_w under the following assumptions:

$$\delta p_{1R}(0, y) = \delta p_{1R}(x_w, y) = 0, \quad (28)$$

$$T_m(x) = T_a + (T_w - T_a)x/x_w, \quad (29)$$

$$\delta T_m(x, y)/T_a = f(y) \sin(\pi x/x_w) \quad (30)$$

where $f(y)$ is a yet unknown function of y . Equation (28) is again a statement that the space at the ends of the regenerator is open enough so that it cannot support a transverse pressure gradient. Equation (29) approximates the streaming-free mean temperature profile as linear. The selection of the sinusoidal behavior of δT_m in Eq. (30) is not based on a rigorous solution of the governing equations. Instead, this particular functional form

simplifies the computation, provides a close representation of the experimentally measured mean temperature deviation when nonzero acoustic streaming is present,¹⁵ and satisfies the boundary conditions $\delta T_m(0, y) = \delta T_m(x_w, y) = 0$. The result of integrating Eq. (27) from $x = 0$ to $x = x_w$ is

$$\delta u_{1R}(0, y) = -\frac{f(y)u_{1R}(0)}{\pi} \frac{2\Gamma + \beta(\tau, b)}{(\tau^{b+2} - 1)/[(\tau - 1)(b + 2)] + (\tau + 1)\Gamma}, \quad (31)$$

where $\tau = T_w/T_a$ and

$$\beta(\tau, b) = (1 + b) \int_0^\pi [1 + (\tau - 1)z/\pi]^b \sin z \, dz \quad (32)$$

This result combined with Eq. (23) and the assumed form of $\delta T_m(x, y)$ given in Eq. (30) gives a complete solution for $\delta u_{1R}(x, y)$ in terms of the streaming-free variables and the unknown function $f(y)$.

Next, we consider the streaming-velocity perturbation $\delta u_{20}(x, y)$ by investigating the second-order, time-average mass-flux density perturbation $\delta \dot{m}_{20}$. In contrast to \dot{m}_{20} , it is not obvious from the outset that $\delta \dot{m}_{20}$ is a constant throughout the regenerator. Considering only $\delta \dot{m}_{20}$, conservation of energy to linear order in the perturbation yields

$$(1 - \phi)\rho_s c_s \epsilon \delta T_m = -\phi c_p \frac{\partial(T_m \delta \dot{m}_{20})}{\partial x}, \quad (33)$$

where the heat capacity of the gas, $\phi \rho_m c_p$, has been ignored relative to the heat capacity of the regenerator screen, $(1 - \phi)\rho_s c_s$. As the local mean temperature of the regenerator changes in time, the local gas density will also change, i.e. $\epsilon \delta T_m \approx -\epsilon T_m \delta \rho_m / \rho_m$. Conservation of mass at linear order in the perturbation requires that the change in local density is fulfilled by a gradient in $\delta \dot{m}_{20}$,

$$-\epsilon \delta \rho_m = \frac{\partial \delta \dot{m}_{20}}{\partial x}. \quad (34)$$

Combining Eqs. (33) and (34) and the discussion in between yields

$$\frac{1}{\delta \dot{m}_{20}} \frac{\partial \delta \dot{m}_{20}}{\partial x} = -\varepsilon \frac{1}{T_m} \frac{\partial T_m}{\partial x} / (1 + \varepsilon), \quad (35)$$

where $\varepsilon = \phi \rho_m c_p / (1 - \phi)\rho_s c_s$. In efficient regenerators, $\varepsilon \ll 1$, and therefore, the change in $\delta \dot{m}_{20}$ with x from one side of the regenerator to the other is small.

Using Eq. (13) as the general definition of \dot{m}_{20} , and with $\dot{m}_{20} = 0$ in the steady state, one expression for $\delta \dot{m}_{20}$ is

$$\delta \dot{m}_{20} = \frac{\rho_m}{2p_m} p_{1R} u_{1R} \left[\frac{\delta u_{1R}}{u_{1R}} - \frac{\delta u_{20}}{u_{20}} \right], \quad (36)$$

where the $\delta p_{1R}/p_{1R}$ term has been ignored because Eqs. (27), (30), and (31) show that it is smaller than the other two terms by a factor $[p_{1R}(0) - p_{1R}(x_w)]/p_{1R}(0)$. Recognizing that $\delta \dot{m}_{20}$ and the prefactor on the RHS of Eq. (36) are approximately independent of x , and using Eqs. (8) and (22), it can be shown that

$$\frac{\delta u_{20}(x, y)}{u_{20}(x)} = \frac{\delta u_{20}(0, y)}{u_{20}(0)} + \frac{\delta T_m(x, y)}{T_m(x)}. \quad (37)$$

To complete the solution for $\delta u_{20}(x, y)$, its value at $x = 0$ still needs to be determined from the, second-order, time-averaged Navier-Stokes equation. We begin by substituting the full solution from Eqs. (15)-(17), but with $\delta u_{1I} = 0$ and $\delta p_{1I} = 0$ as established above, into the time-dependent, spatially-averaged Navier-Stokes equation for screens,¹⁴ expanding to first order in the perturbation, expanding the linear term to second order in the acoustic amplitude and the nonlinear term to third order, and time averaging. An intermediate result is

$$\begin{aligned} -\frac{\partial \delta p_{20}}{\partial x} = & \frac{c_1 \mu_m u_{20}}{8r_h^2} \left[\frac{\delta u_{20}(0)}{u_{20}(0)} + (1+b) \frac{\delta T_m}{T_m} \right. \\ & \left. + \frac{4c_2 N_R}{3\pi c_1} \left(\frac{3\delta u_{20}(0)}{u_{20}(0)} - \frac{\delta u_{1R}(0)}{u_{1R}(0)} + \frac{\delta T_m}{T_m} - \frac{2\delta p_{1R}}{p_{1R}} \text{ plus } u_{22} \text{ and } \delta u_{22} \text{ terms} \right) \right] \end{aligned} \quad (38)$$

For the reason given below Eq. (36), the $\delta p_{1R}/p_{1R}$ can be dropped. However, the terms proportional to u_{22} and δu_{22} are more problematic. By assuming the density oscillations at 2ω are still isothermal, it can be shown that $u_{22}(x) = u_{22}(0)[T_m/T_a]$, but $u_{22}(0)$ is still undetermined. In an OPTR, adjustments to the driving piston's motion could be made to force $p_{22}(0) = p_{22}(x_w)$, but, this may not ensure that $u_{22}(0)$ is actually zero because the nonlinearities in the regenerator, at interfaces between components, and due to finite motion of the piston itself are continually generating 2ω terms throughout the system. Without knowledge of u_{22} , there is no way to calculate δu_{22} . The only way to close the equations without introducing a whole host of additional equations that address these nonlinearities is to simply drop the u_{22} and δu_{22} .

To extract $\delta u_{20}(0)$, Eq. (38) is integrated from $x = 0$ to x_w . Assuming that the spaces at the two ends of the regenerator are open enough to disallow a transverse pressure gradient, the integral of the LHS of Eq. (38) is zero. Using Eqs. (14), (29)-(31), and the temperature

dependence of μ_m , the result of integrating Eq. (38) is

$$\delta u_{20}(0) = - \frac{f(y)u_{20}(0)/\pi}{(\tau^{b+2} - 1)/[(b+2)(\tau-1)] + 3(\tau+1)\Gamma/4} \times \left[\frac{\Gamma(\tau+1)[2\Gamma + \beta(\tau, b)]/4}{(\tau^{b+2} - 1)/(b+2)(\tau-1) + (\tau+1)\Gamma} + \beta(\tau, b) + \Gamma \right] \quad (39)$$

Equations (14), (29), (30), (37), and (39) provide a full solution for $\delta u_{20}(x, y)$.

With solutions for δu_{1R} and δu_{20} in hand, the calculation can proceed to the energy equation, which reveals the origin of the instability. Simplified for the two-dimensional geometry considered here, the energy equation is given by

$$(1 - \phi)\rho_s c_s \frac{\partial}{\partial t} \left[T_s + \frac{\phi \rho c_v}{(1 - \phi)\rho_s c_s} T \right] = - \frac{\partial \dot{h}_x}{\partial x} - \frac{\partial \dot{h}_y}{\partial y} \quad (40)$$

where T_s , c_s , and ρ_s are the temperature, heat capacity, and density of the regenerator solid matrix, respectively. In good regenerators, $\phi \rho c_v / (1 - \phi)\rho_s c_s \ll 1$ so the second term in the square brackets can be safely ignored. On the slow time scale of the initial growth of the perturbation, the heat transfer between the regenerator solid and the gas is adequate to ensure $\partial T_s / \partial t \approx \epsilon \delta T_m$. Using these approximations, substituting the full solution into Eq. (40), and expanding to first order in the perturbation yields

$$(1 - \phi)\rho_s c_s \epsilon \delta T_m = - \frac{\partial \delta \dot{h}_x}{\partial x} - \frac{\partial \delta \dot{h}_y}{\partial y} \quad (41)$$

Since we have assumed there are no acoustic or streaming flows in the y direction, the energy flux perturbation along y can be written

$$\frac{\partial \delta \dot{h}_y}{\partial y} = -k_y \frac{\partial^2 \delta T_m}{\partial y^2} = -k_y T_a \sin(\pi x / x_w) \frac{d^2 f(y)}{dy^2}. \quad (42)$$

Here, k_y is the effective thermal conductivity of the regenerator solid in the y direction, which is much lower than the thermal conductivity of the regenerator solid, k_s , for three reasons. First, the screen wires do not fill up the entire cross-sectional area of the screen. Second, the length of a piece of wire between two points is longer than the distance between the points due to the sinewave-like bending of the wire as it passes over and under the wires running in the perpendicular direction. Third, the wires are not all aligned with the direction of heat flow. Taking all of these effects into account, k_y is given by

$$k_y = \frac{1 - \phi}{2K(\phi)} k_s \quad (43)$$

where

$$K(\phi) = \frac{2}{\pi} \int_0^{\pi/2} \sqrt{1 + 4(1 - \phi)^2 \sin^2 z} dz. \quad (44)$$

Applying the simplifications mentioned above, substituting Eqs. (30) and (42) into Eq. (41) and integrating from $x = 0$ to x_w yields an expression for the growth rate ϵ

$$(1 - \phi)\rho_s c_s f(y)\epsilon = \frac{\pi}{2x_w} \frac{[\delta\dot{h}_x(0) - \delta\dot{h}_x(x_w)]}{T_a} + k_y \frac{d^2 f(y)}{dy^2}. \quad (45)$$

To complete the calculation, we only need to express $\delta\dot{h}_x(0)$ and $\delta\dot{h}_x(x_w)$ in terms of δT_m , i.e. in terms of $T_a f(y)$.

The streaming-free solution for the energy flux along x is given by $\dot{h}_x = \langle \tilde{m}_x c_p \tilde{T} \rangle - k_x \partial T / \partial x$, where k_x is the effective conductivity of the screen in the x direction.^{14,16} Here, we have been forced to deviate from our original variable definitions by the form of the expression for \dot{h} . Variables with a tilde are microscopically varying¹⁴ and $\langle \dots \rangle$ indicates a local spatial average including a reasonable number of pores. Time averaging, expanding to linear order in the perturbation, and realizing that we only need the energy flux at $x = 0$ or x_w yields

$$\dot{h}_{2,x} = \dot{m}_{1R} c_p \langle \tilde{T}_{1R} \rangle_{\tilde{u}_{1R}} / 2 - k_x \partial T_m / \partial x \equiv \dot{h}_c + \dot{h}_k, \quad (46)$$

$$\delta\dot{h}_x = \dot{h}_c \left[\frac{\delta u_{1R}}{u_{1R}} + \frac{\langle \delta \tilde{T}_{1R} \rangle_{\tilde{u}_{1R}}}{\langle \tilde{T}_{1R} \rangle_{\tilde{u}_{1R}}} \right] + \dot{h}_k \left[\frac{\partial \delta T_m / \partial x}{\partial T_m / \partial x} \right] + \delta \dot{m}_{20} c_p T_m, \quad (47)$$

We have again deviated somewhat from our original definitions of T_1 and δT_1 by working with velocity-weighted averages,¹⁴ such as $\langle \tilde{T}_{1R} \rangle_{\tilde{u}_{1R}} = \langle \tilde{T}_{1R} \tilde{u}_{1R} \rangle / \langle \tilde{u}_{1R} \rangle$, instead of simple spatial averages. In the derivation of Eq. (47), we have assumed $\langle \tilde{T}_{1R} \rangle_{\tilde{\delta u}_{1R}} = \langle \tilde{T}_{1R} \rangle_{\tilde{u}_{1R}}$; this seems plausible since both \tilde{u}_{1R} and $\tilde{\delta u}_{1R}$ flow through the same regenerator matrix and should experience similar small-scale spatial fluctuations.

The temperature oscillations are computed from Eq. (27) of Swift and Ward,¹⁴ where they assume that the heat capacity of the regenerator solid is much larger than that of the gas and the gas-to-regenerator heat-transfer coefficient h does not depend on Reynolds number. We make the additional simplification that $\omega \rho_m c_p / (h/r_h) \approx (r_h/\delta_\kappa)^2 \ll 1$. The result is

$$\langle \tilde{T}_{1R} \rangle_{\tilde{u}_{1R}} = - \frac{\rho_m c_p u_{1R} (\partial T_m / \partial x)}{h/r_h}. \quad (48)$$

Substituting the full solution into Eq. (27) of Swift and Ward¹⁴ and expanding to first order

in the acoustic variables and linear order in the perturbation, we find

$$\langle \delta \tilde{T}_{1R} \rangle_{\tilde{u}_{1R}} = \langle \tilde{T}_{1R} \rangle_{\tilde{u}_{1R}} \left[\frac{\delta u_{1R}}{u_{1R}} + \frac{\partial \delta T_m / \partial x}{\partial T_m / \partial x} \right], \quad (49)$$

where we have again assumed $\langle \tilde{T}_{1R} \rangle_{\tilde{\delta} u_{1R}} = \langle \tilde{T}_{1R} \rangle_{\tilde{u}_{1R}}$. In Eq. (49), we have dropped a term proportional to $\delta \rho_m$ because $\langle \delta \tilde{T}_{1R} \rangle_{u_{1R}}$ is only needed at $x = 0$ and x_w where $\delta \rho_m$ is zero.

Substituting Eqs. (23), (30), (47), and (49) into Eq. (45) we find

$$\frac{2x_w}{\pi} (1 - \phi) \rho_s c_s T_a \epsilon f(y) = \frac{2\pi \dot{h}_{2,x} f(y)}{\tau - 1} + \delta \dot{m}_{20} c_p T_a (1 - \tau) + \frac{2x_w k_y T_a}{\pi} \frac{d^2 f(y)}{dy^2}, \quad (50)$$

To arrive at this result, the two terms of $\dot{h}_{2,x}$, \dot{h}_c and \dot{h}_k , are each taken to be independent of x . Equations (22), (30), (31), (36), (37), and (39) can be combined to show that $\delta \dot{m}_{20}$ is proportional to $f(y)$, so Eq. (50) shows that $f(y)$ is proportional to $\sin(n\pi y/y_w)$ or $\cos(n\pi y/y_w)$. The value of n is constrained by the temperature boundary conditions imposed by the regenerator geometry. For example, n is even for annular regenerators of circumferential extent y_w , to force continuity of temperature. (The requirement that $\int \delta \dot{m}_{20} dy = 0$ rules out $n = 0$.) Substituting Eq. (36) evaluated at $x = 0$ into Eq. (50) and using the ideal gas equation of state, we find

$$\begin{aligned} \frac{x_w y_w z_w (1 - \phi) \rho_s c_s T_a}{\pi^2 E_a} \epsilon = & - \frac{(H/E_a)}{1 - \tau} - n^2 \frac{k_y T_a z_w x_w / y_w}{E_a} \\ & + \frac{\gamma}{\gamma - 1} \frac{1 - \tau}{2\pi} \left(\frac{\delta u_{1R}(0)}{u_{1R}(0)} - \frac{\delta u_{20}(0)}{u_{20}(0)} \right) / f(y). \end{aligned} \quad (51)$$

Here, H and E_a are the total energy flux and the total acoustic power flux at the ambient end of the regenerator, z_w is the short dimension of the regenerator transverse to x_w , and γ is the ratio of specific heats of the working gas.

Equation (51) begins to shed some light on when an instability may arise. All factors on the LHS of Eq. (51), other than perhaps ϵ itself, are positive. Therefore, the sign of ϵ is determined only by the RHS of the equation. The transverse conductivity term, the term proportional to k_y , is negative for both engines and refrigerators and, therefore, always contributes to the stability of the streaming and temperature distribution. It is proportional to n^2 , so it selects the broadest possible mode for the instability: $n = 2$ for our annular regenerator, $n = 1$ for a wide rectangular regenerator. (For circular regenerators, $f(y)$ would be something like $J_0(kr) \cos(n\theta)$ with k such that $(d/dr)J_0(kr) = 0$ at the circumference of the regenerator, and $n = 1$ would be selected.) For engines, $\tau > 1$, $E_a > 0$, and $H < 0$,

making the first term on the RHS negative. In refrigerators, $\tau < 1$, $E_a > 0$, and $H > 0$, so the first term is still negative. Therefore, this term always contributes to the stability of the streaming distribution. The third term on the RHS is more difficult to analyze. For values of τ , b , and Γ over the wide range we have explored, the difference inside the parentheses divided by $f(y)$ is always positive. Therefore, for engines, the third term on the RHS is always negative and this calculation predicts that engines are inherently immune from streaming instabilities. However, for refrigerators, the third term on the RHS is positive, leading to the possibility of a streaming instability. In the case of refrigerators, a streaming instability will arise (i.e. $\epsilon > 0$) when

$$\frac{H}{E_a} < \frac{\gamma}{\gamma - 1} \frac{(1 - \tau)^2}{2\pi} \left(\frac{\delta u_{1R}(0)}{u_{1R}(0)} - \frac{\delta u_{20}(0)}{u_{20}(0)} \right) / f(y) - n^2(1 - \tau) \frac{k_y T_a z_w x_w}{y_w} / E_a, \quad (52)$$

with $\delta u_{1R}(0)/f(y)u_{1R}(0)$ given by Eq. (31) and $\delta u_{20}(0)/f(y)u_{20}(0)$ given by Eq. (39). One interesting result is that for a regenerator with a linear flow resistance, i.e. $c_2 = 0$ in Eq. (26), $\Gamma = 0$, $\delta u_{1R}(0)/u_{1R}(0) = \delta u_{20}(0)/u_{20}(0)$, and there is no instability of the type described here. The conclusion is that a parallel plate regenerator with uniform plate spacing and a Reynolds number less than about 2000 does not suffer from this type of instability.

III. APPARATUS

Since the acoustic streaming instability is sometimes expected in refrigerators but never in engines, we have built an orifice pulse tube refrigerator (OPTR) to specifically search for it. Figure 2 shows a scale drawing of the OPTR used in these measurements. It consists of three heat exchangers, a regenerator, and a pulse tube. The rest of the hardware includes a piston driven by a linear motor,¹⁷ an experimental offset, and a variable acoustic network. The system is filled with 30-bar helium gas and driven at a fixed frequency of 45 Hz. The 0.10-m diameter piston (not shown) is located directly beneath the experimental offset.

The offset is simply an open cylinder that allows for impedance matching between the OPTR and the piston/linear motor. It also allows access to the inner cooling-water channel of the aftercooler. The offset also has a port for measuring acoustic pressure using a piezoresistive transducer.¹⁸

Above the offset is the aftercooler, which is the principal ambient heat exchanger. It is made from a 5.1-cm-thick brass block drilled with a total of 90 3.2-mm-diameter holes in

two circular rows. Annular cooling-water channels are located just inboard and outboard of the holes.

Above the aftercooler is the regenerator. It is made from plain square-weave stainless-steel screen with an inner diameter of 5.5 cm and outer diameter of 7.4 cm. The screen is cut by wire electrical-discharge machining, cleaned, and then packed into the regenerator housings with an annular die to a height of $x_w = 5.08$ cm. The inner and outer housings around the regenerator have wall thicknesses of 1.65 and 1.32 mm, respectively. On each end, four layers of 20-mesh copper screen with a wire diameter of 0.4 mm are inserted as simple spacers to allow room for the flow to spread out after exiting the heat exchangers. Temperatures are measured with forty 1.0-mm-diameter sheathed type-K thermocouples located every 45° around the azimuth at the five axial positions as shown in Fig. 2. The thermocouples are inserted into tight-fitting pockets drilled halfway through the regenerator's annular thickness, and the stainless-steel sheaths are soft soldered to slightly larger, short tubes that are brazed to the outer housing, thereby making a leak-tight seal. The top and bottom sets of eight are centered in the copper spacers. The other three sets are in the regenerator itself, just inside the copper spacers and at the axial midpoint.

Two different regenerators are tested. The first has a porosity of 0.686 and a hydraulic radius⁸ of $22.2 \mu\text{m}$. The second has a porosity of 0.686 and a hydraulic radius of $13.9 \mu\text{m}$. In both regenerators, the hydraulic radius is much smaller than the thermal penetration depth, about $204 \mu\text{m}$ at 300 K, ensuring good thermal contact between the helium gas and the screen. The first regenerator never showed an instability. Data from it are only discussed briefly, and the rest of this article focuses on the second regenerator.

Above the regenerator is the cold heat exchanger. It is made from a 1.9-cm-thick block of OFHC copper drilled with a total of 180 2.4-mm-diameter holes in three circular rows. A channel around the outside of the heat exchanger allows for cooling or heating of the heat exchanger with liquid or gaseous nitrogen or a water–antifreeze mixture as necessary. Eight type-K thermocouples are inserted into drilled pockets around the perimeter near the lower face of the cold heat exchanger at the same angular locations as in the regenerator.

The annular pulse tube is located above the cold heat exchanger. Its stainless-steel inner and outer shells are nearly identical to the regenerator housings. The pulse tube provides thermal insulation between the cold and ambient heat exchangers while transmitting acoustic power out of the cold zone. The surfaces facing the helium gas are polished to ensure

that the surface roughness is much less than the viscous and thermal penetration depths. Several layers of copper screen at either end of the pulse tube serve as flow straighteners. Temperature in the pulse tube is measured with 16 type-K thermocouples spot welded to the outer wall every 45° around the azimuth at two axial locations.

Above the pulse tube is the secondary ambient heat exchanger, which is similar in construction to the aftercooler. It consists of a drilled brass block with a cooling-water channel around its outside. Next, an annular manifold and four 6.4-mm-diameter tubes adapt the annular geometry back to a tubular geometry. A flow straightener in the manifold keeps the flow from the four tubes from jetting through the secondary ambient heat exchanger. A second acoustic pressure sensor is located in the manifold.

Above the four adapter tubes, 3.4 m of 12.7-mm-diameter inertance tubing extends to a 2.3-liter compliance tank forming an acoustic network¹⁹ used to set the volumetric flow rate at the aftercooler. A third pressure sensor is located in compliance. All three pressure sensors are calibrated using a steady pressure measured with a NIST-traceable Bourdon-tube pressure gauge.

IV. PRELIMINARY MEASUREMENTS

Several quantities must be measured accurately to make a comparison with the theory: τ , Γ , E_a , H , and k_y . For the first three of these, we require accurate measurements of the temperature, complex pressure p_{1a} , and volumetric velocity U_{1a} at the ends of the regenerator.

Thermocouples in the copper spacers, regenerator, cold heat exchanger, and pulse tube are calibrated *in situ* by submerging the entire assembly in baths of known temperature: liquid nitrogen (75 K at Los Alamos atmospheric pressure) and a dry ice–acetone bath (195 K). A third calibration point is obtained by letting the insulated system sit undisturbed overnight (with the cooling water shut off) and reading all of the thermocouples in the morning. Quadratic fits to the temperature deviations are used to interpolate the corrections between the calibration points. The range of the temperature corrections is ± 3 K and ± 8 K at dry ice–acetone and liquid-nitrogen temperatures, respectively.

The measurement of the complex pressure amplitude is straightforward. All pressure sensors in the OPTR are read out with the same lock-in amplifier, ensuring accurate magnitude

and phase information. The magnitude and phase of the pressure amplitude in the experimental offset changes very little along its length, so the pressure measured at this sensor provides the complex pressure amplitude at both the piston face, $p_{1,p}$, and the ambient end of the regenerator, $p_{1,a}$.

The complex volumetric-velocity amplitude is more difficult to determine. A mutual-inductance-based linear variable-displacement transducer (LVDT)²⁰ on the linear motor provides a measure of the complex displacement amplitude of the piston. The flow rate at the piston face, $U_{1,p}$, is then determined from knowledge of the piston area and angular frequency of the oscillation, ω . However, U_1 changes significantly between the piston face and the ambient face of the regenerator. Most of the change is in the imaginary part and is due to the compliance of the experimental offset. This change is easily accounted for by measuring the total volume between the piston face and the aftercooler, and knowing ω , $p_{1,a}$, and the mean pressure. However, there is also a change in the real part of U_1 due to thermal and viscous dissipation on the experimental offset wall, E_{offset} , as well as dissipation due to leakage through the clearance seal between the compressor's piston and cylinder, E_{seal} . Instead of trying to compute each source of dissipation, a set of measurements is carried out to determine the combined effect of all of them. At the top of the experimental offset, the OPTR is replaced by a variable acoustic load consisting of a 2.2-liter tank connected to the offset by a water-cooled globe valve.²¹ By adjusting the valve, varying amounts of acoustic power, E_{load} , can be dissipated in the load. Pressure sensors in the tank and offset are used to obtain E_{load} .²¹ The acoustic power leaving the piston face, E_p , is determined from measurements of $U_{1,p}$ using the LVDT and $p_{1,a}$ using the pressure sensor in the experimental offset. Both measurements are made using the lockin amplifier, which allows for accurate determination of the phase between $p_{1,a}$ and $U_{1,p}$. With the load valve closed, $E_p = E_{\text{offset}} + E_{\text{seal}}$. As the load valve is opened, the additional power drawn by the load must originate at the piston face. Therefore, $E_p = E_{\text{offset}} + E_{\text{seal}} + E_{\text{load}}$. If $p_{1,a}$ is held constant for each valve setting, E_{seal} and E_{offset} should be nearly constant. Therefore, if E_p is plotted versus E_{load} for various valve settings, the result should be a straight line of slope 1 and an E_p -axis intercept of $E_{\text{offset}} + E_{\text{seal}}$. Figure 3 shows the results of these measurements. Each set of data is fitted with a straight line, and the slopes range from 1.00 to 1.05 demonstrating the accuracy of the E_p and E_{load} measurements. The fitted intercepts giving $E_{\text{offset}} + E_{\text{seal}}$ are displayed in Fig. 4.

The entire system is modeled with DeltaE.²² To account for the dissipation in the piston seal and experimental offset, an extra side-branch acoustic resistance that dissipates $E_{\text{seal}} + E_{\text{offset}}$ from Fig. 4 is added to the DeltaE model at the piston-end of the experimental offset. In combination with a segment that models the compliance of the offset, the extra resistance makes appropriate changes to $U_{1,p}$ to give $U_{1,a}$, which also modifies E_p to give E_a . For each data point, measurements of $U_{1,p}$, $p_{1,a}$, $p_{1,\text{net}}$, and $p_{1,t}$ are compared with calculations using the DeltaE model. Here, $p_{1,\text{net}}$ and $p_{1,t}$ are the complex pressure amplitudes in the ambient manifold just below the acoustic network and in the compliance tank, respectively. Typical results are shown in Fig. 5. The phase of $p_{1,a}$ has been arbitrarily set to zero, and $|p_{1,a}|$ is forced to be the same in the model and experiment. The measured $U_{1,p}$ phasor is in good agreement with the model. The only other measure of U_1 in the system is the pressure oscillation in the compliance tank. The good agreement between the measurement of $p_{1,t}$ and the model indicates U_1 into the tank is close to the model predictions. With agreement between measurement and model predictions for U_1 at the piston and in the compliance tank, the model predictions of $U_{1,a}$ (which determines Γ) and U_1 throughout the system can be used with some confidence.

In principle, the total energy flux H through the regenerator could be determined from the difference between E_a and the measured heat rejected at the aftercooler. However, this would not provide a very accurate measure because H is relatively small compared to both of these quantities. Therefore, we resort to our knowledge of U_1 and p_1 throughout the system to numerically compute²² H . However, for this computation to be accurate, we must know the flow impedance and heat-transfer properties of the regenerator, which depend on r_h and ϕ . By measuring the total mass of the screen in the regenerator and its volume, ϕ is accurately determined. The hydraulic radius is determined from ϕ and the diameter of the screen wire, d_w , as quoted by the manufacturer, via $r_h = (d_w/4)\phi/(1 - \phi)$, yielding 13.9 μm for the second regenerator. The acoustic pressure drop across the OPTR, $p_{1,a} - p_{1,\text{net}}$, is used as a check of this value of r_h . Figure 5 shows the typically 80% agreement between the measurements of $p_{1,a} - p_{1,\text{net}}$ and the numerical computation.²² A 20% uncertainty in $p_{1,a} - p_{1,\text{net}}$ implies a 10% uncertainty in r_h , which in turn implies a 20% uncertainty in our computed values of H .

V. EXPERIMENTS

To search for the instability, we vary the ratio H/E_a . We interpret any azimuthal dependence of the steady-state temperature in the mid plane of the regenerator as a sign that an instability has arisen, has grown in time, and has stopped growing when it reaches a balance with some other nonlinear effect that is beyond the scope of this paper. Data are taken by keeping both T_a and T_w (i.e. τ) nearly fixed while varying $|p_{1,a}|$. Under these conditions, E_a goes approximately as $|p_{1,a}|^2$. The hydrodynamically transported energy flux \dot{h}_c in Eq. (46) also grows as $|p_{1,a}|^2$. However, \dot{h}_k , the thermal-conduction component of the energy flux in Eq. (46), stays fixed. Therefore, by varying $|p_{1,a}|$, we can vary H/E_a in Eq. (52) while keeping τ fixed. At each acoustic amplitude, the system is allowed to reach a steady state indicated by negligible changes in temperature of any of the thermocouples in the regenerator. All the thermocouple temperatures, the acoustic pressures, and the piston amplitude are then recorded. The temperatures at the ambient and cold end of the regenerator and $|p_{1,a}|$ are used as inputs to the numerical model that calculates H . The acoustic power E_a is determined as described in the previous section.

At low amplitude where H is dominated by \dot{h}_k and H/E_a is large, the temperature at the axial midpoint of the regenerator is found to be roughly independent of azimuthal angle. As $|p_{1,a}|$ is increased, the angular temperature distribution changes little until a critical $|p_{1,a}|$ is reached, where a sinewave-like angular temperature distribution appears. If $|p_{1,a}|$ is increased beyond the critical value, the amplitude of the temperature variation increases. A typical set of data for $T_a \approx 300$ K and $T_c \approx 77$ K is shown in Fig. 6. Here, the temperature at the axial midpoint at each angle, $T_{\text{mid},n}$ is normalized by the temperatures at the ambient and cold ends, $T_{a,n}$ and $T_{c,n}$ respectively, by

$$\Delta_n = \frac{T_{\text{mid},n} - (T_{a,n} + T_{c,n})/2}{T_{a,n} - T_{c,n}} - Z_n. \quad (53)$$

Any residual bias from systematic errors in the thermocouple calibration is removed by subtracting off from each Δ_n a zero Z_n which is obtained by averaging data sets whose $|p_{1,a}|$ are clearly below the critical value. The resulting Δ_n values are plotted in Fig. 6 for several $|p_{1,a}|$. A numerical calculation indicates that a sinusoidally y -dependent streaming mass flux with a peak of only $0.003 \text{ Re}[\rho_1 u_1^*]/2$ would cause the changes in temperature observed at $|p_1/p_m| = 0.08$.

To accurately determine the location of the transition to streaming, the magnitude of the temperature variation in Fig. 6 is determined from a Fourier transform via

$$|A|^2 = \left| \frac{\pi}{4} \sum_{n=1}^8 \Delta_n \cos(n\pi/4) \right|^2 + \left| \frac{\pi}{4} \sum_{n=1}^8 \Delta_n \sin(n\pi/4) \right|^2, \quad (54)$$

and $|A|^2$ is plotted versus E_a/H in Fig. 7. Consistent with Eq. (52), as E_a/H becomes larger a critical value is reached where $|A|^2$ begins to rapidly grow. There is some rounding near the transition, and the critical value $(E_a/H)_{crit}$ is defined as the $|A|^2 = 0$ intercept of a line fitted to the data points beyond the visible rounding.

The same data taking and analysis procedure is applied to data sets with $T_a \approx 300$ K and T_c spanning 77 K to 285 K. The results for $(H/E_a)_{crit}$ versus τ are plotted as the circles in Fig. 8. The detailed acoustic and thermal conditions are shown in Table I. Operating conditions above and to the right of the circles in Fig. 8 do not show azimuthal temperature variations, whereas operating conditions below and to the left of the circles show azimuthal variations presumably due to the acoustic streaming instability described earlier. The first regenerator, with a 22.2 μm hydraulic radius, always yielded a higher (H/E_a) for a particular τ , i.e. above and to the right of the data points in Fig. 8, and never showed an instability.

Comparing the experimental results in Fig. 8 with Eq. (52) is not straightforward because τ is not the only independent parameter on the right hand side of Eq. (52). The other independent parameter is Γ , which is a measure of the Reynolds number at the ambient end of the regenerator. Experimentally, Γ can be varied by using a valve (not shown in Fig. 2) in the acoustic network to vary the impedance of the network. However, increasing Γ by a factor of two is not feasible because the pressure drop across the regenerator would become comparable to $|p_{1,a}|$, violating one of the assumptions in the calculation. Decreasing Γ by a factor of two is also not possible for several reasons. First, lower values of Γ imply smaller $|U_{1,a}|$ at the same $|p_{1,a}|$. The consequence would then be large phase shifts in U_1 from the ambient to cold end of the regenerator, violating our assumption that p_1 and U_1 are in phase throughout the regenerator. Second, to maintain the phase of $p_{1,a}$ relative to $U_{1,a}$ near zero would require an acoustic network that had nearly the same inertial component (i.e. reactive component) while reducing the dissipative component by a factor of two. This is not possible at the current power level. Therefore, we are restricted to the narrow range of Γ allowed by the current apparatus.

In Fig. 8, experimental values of Γ range from about 0.35 at the lowest τ to 0.15 at the

highest. The variation in Γ is somewhat subtle. At a particular $|p_{1,a}|$, the volumetric flow rate at the cold end of the regenerator, $U_{1,c}$, is fixed by the dimensions of the inertance tube and the compliance tank. Equation (8) shows that $U_{1,a} = U_{1,c}/\tau$. Therefore, $U_{1,a}$ and Γ are smaller for large τ and larger for small τ . Instead of calculating an instability threshold for each data point, we present two curves in Fig. 8; one for the threshold with $\Gamma = 0.35$ and another for $\Gamma = 0.15$. To help distinguish the magnitude of the two contributions on the right hand side of Eq. (52), the bold curves only take into account the first term while the thin curves also take into account the transverse conduction term. Just as with the experimental data, operating points below and to the left of the curves are unstable while those above and to the right are stable.

The qualitative agreement between measurements and calculations in Fig. 8 is encouraging. Both experiment and calculation show an instability for operation below a critical value of H/E_a , and both show that $(H/E_a)_{\text{crit}}$ decreases as τ increases. However, the quantitative agreement is not very good. As the bold curves show, the disagreement is not simply due to an overestimate of the stabilizing effect of transverse conduction. Instead, we may be underestimating the destabilizing effects of streaming or simply leaving out one or more important effects. The exact solutions for oscillating flow and heat transfer in a screen regenerator are unknown, forcing us to use steady-flow correlations in a oscillating flow.¹⁴ Inaccuracies certainly result, and the effects on this subtle calculation are difficult to estimate. In addition, since we cannot solve the equations for the perturbation exactly, we have assumed the functional form of the temperature perturbation profile based on observations of a different system when streaming was present. Although we believe this form to be close to reality, perhaps the instability threshold would be significantly changed by picking a different functional form. The calculation we have presented assumes that p_1 and U_1 are in phase throughout the regenerator. The data in Table 1 show that $U_{1,a}$ leads $p_{1,a}$ by approximately 40° . The effect of this phase difference is difficult to estimate without including it at all stages of the calculation. Finally, we assumed the *transverse* acoustic and streaming velocity perturbations are both zero. In reality this is certainly not the case because, although not presented in this paper, the solutions arrived at in this calculation show a y -dependent p_1 and $p_{2,0}$ inside the regenerator, i.e. everywhere but $x = 0$ or $x = x_w$. Quick initial estimates show that the energy flows driven by the resulting transverse acoustic and streaming flows are either stabilizing or have no effect. However, more detailed calculations

are required to verify these estimates.

VI. CONCLUSIONS

A calculation has been presented showing that an acoustic streaming instability can arise in the regenerators of oscillating-wave refrigerators, while engines are immune. The calculation begins by assuming that a region ‘A’ near the midplane of the regenerator becomes a little hotter than it should while region ‘B’ (also near the midplane but some transverse distance away) becomes a little cooler. Some of the consequences of such a mean temperature perturbation will always remove heat from region A and deposit heat in region B, leading to a suppression of the original perturbation. Referring to Eq. (51), these include transverse thermal conduction through the regenerator screen (proportional to k_y) and the axial total energy flux H (proportional to dT_m/dx). The other term in Eq. (51), $\delta u_{1R}(0)/u_{1R}(0) - \delta u_{20}(0)/u_{20}(0)$, is proportional to the second-order streaming mass-flux perturbation. Under all conditions we have explored, the resulting steady mass flux is always positive (i.e. directed from T_a to T_w in regions where the midplane temperature is higher). In engines, heat is extracted from region A and deposited in region B by this term, which suppresses the mean temperature perturbation and leads to the stability of engines to this type of perturbation. However, the opposite is true in refrigerators where additional heat is deposited in the region A and removed from region B. The details of the state of the refrigerator’s regenerator dictate whether the heat flux perturbation due to this streaming can overcome the stabilizing effects of transverse thermal conduction and axial total energy flux. If it does, the perturbation grows, resulting in an instability in refrigerators.

When a perturbation is present, the changes in the heat flux due to the transverse thermal conduction and the axial energy flux are easily understood. However, the second-order streaming mass-flux perturbation is more complicated. It is nonzero because the nonlinear flow resistance of the regenerator results in different flow resistances for the first-order acoustic flow and the second-order streaming flow and because these resistances change with mean temperature in different ways.

The calculation of the instability threshold is difficult because the three effects mentioned above are all about the same size. A small inaccuracy in the calculation of any one of three can lead to a significant inaccuracy in the result for the instability threshold. An

accurate numerical calculation could presumably predict the instability threshold. However we chose to attempt an analytical calculation to gain understanding by identifying the specific stabilizing and destabilizing mechanisms.

An orifice pulse tube refrigerator with a well-instrumented regenerator was built to determine the instability threshold. The calculation described above and the experimentally determined threshold show qualitative agreement, but quantitative agreement is still lacking. Possible routes of additional theoretical investigation include better models for the flow and heat transfer in regenerators, determining the exact solution for the x dependence of the mean-temperature perturbation, and including acoustic and streaming flow transverse to the main acoustic axis.

Acknowledgments

The authors would like to acknowledge D. Gardner for work on an early version of this experiment, C. Espinoza for his expert assistance in the construction of the experiment, and the Office of Basic Energy Sciences within the U.S. DOE Office of Science for financial support.

* Electronic address: backhaus@lanl.gov

- ¹ A. J. Organ. *The Regenerator and the Stirling Engine*. Mechanical Engineering Publications, Ltd., 1997.
- ² R. Radebaugh. A review of pulse tube refrigeration. *Adv. Cryogenic Eng.*, 35:1191–1205, 1990.
- ³ G. W. Swift, D. L. Gardner, and S. Backhaus. Acoustic recovery of lost power in pulse tube refrigerators. *J. Acoust. Soc. Am.*, 105:711–724, 1999.
- ⁴ S. Backhaus and G. W. Swift. A thermoacoustic-Stirling heat engine. *Nature*, 399:335–338, 1999.
- ⁵ T. Yazaki, A. Iwata, T. Maekawa, and A. Tominaga. Traveling wave thermoacoustic engine in a looped tube. *Phys. Rev. Lett.*, 81:3128–3131, 1998.
- ⁶ C. M. de Blok and N. A. H. J. van Rijt, Thermo-acoustic system, U. S. Patent No. 6,314,740, Nov. 13, 2001.
- ⁷ D. L. Gardner and G. W. Swift. A cascade thermoacoustic engine. *J. Acoust. Soc. Am.*, 114:1905–1919, 2003.
- ⁸ A. J. Organ. *Thermodynamics and Gas Dynamics of the Stirling Cycle Machine*. Cambridge University Press, 1992.
- ⁹ David Gedeon. Flow circulation in foil-type regenerators produced by non-uniform layer spacing. In R. G. Ross, editor, *Cryocoolers 13*, pages 421–430. Springer, New York, 1999.
- ¹⁰ C. S. Kirkconnell. Experimental investigation of a unique pulse tube expander design. In R. G. Ross, editor, *Cryocoolers 10*, pages 239–247. Plenum, New York, 1999.
- ¹¹ G. W. Swift. *Thermoacoustics: A unifying perspective for some engines and refrigerators*. Acoustical Society of America, 2002.
- ¹² S. Chandrasekhar. *Hydrodynamic and Hydromagnetic Stability*. Dover, New York, 1961.
- ¹³ S. Backhaus and G. W. Swift. An acoustic streaming instability in thermoacoustic devices utilizing jet pumps. *J. Acoust. Soc. Am.*, 113:1317–1324, 2003.
- ¹⁴ G. W. Swift and W. C. Ward. Simple harmonic analysis of regenerators. *J. Thermophysics and Heat Transfer*, 10:652–662, 1996.
- ¹⁵ Unpublished data measured in a different apparatus (S. Backhaus, E. Tward, and M. Petach. Traveling-wave thermoacoustic generator. *App. Phys. Lett.*, 85:1085–1087, 2004) using 5 ther-

mocouples attached to the outside of a thin-wall can containing the regenerator show that this profile is closely represented by a sinewave.

- ¹⁶ M. A. Lewis, T. Kuriyama, F. Kuriyama, and R. Radebaugh. Measurement of heat conduction through stacked screens. *Adv. Cryogenic Eng.*, 43:1611–1618, 1998.
- ¹⁷ Model C2, Qdrive, Inc., Troy NY, www.qdrive.com.
- ¹⁸ Model 8510B-500. Endevco Corporation, 30700 Rancho Viejo Road, San Juan Capistrano, CA 92675.
- ¹⁹ D. L. Gardner and G. W. Swift. Use of inertance in orifice pulse tube refrigerators. *Cryogenics*, 37:117–121, 1997.
- ²⁰ Schaevitz Model 500 HR, Measurement Specialties, Inc. Fairfield NJ, www.schaevitz.com.
- ²¹ A. M. Fusco, W. C. Ward, and G. W. Swift. Two-sensor power measurements in lossy ducts. *J. Acoust. Soc. Am.*, 91:2229–2235, 1992.
- ²² W. C. Ward and G. W. Swift. Design environment for low amplitude thermoacoustic engines (DeltaE). *J. Acoust. Soc. Am.*, 95:3671–3672, 1994. Software and user’s guide available either from the Los Alamos thermoacoustics website at www.lanl.gov/thermoacoustics/ or from the Energy Science and Technology Software Center, US Department of Energy, Oak Ridge, Tennessee.

Table I. Acoustic and thermal conditions for the data in Fig. 8

T_c (K)	τ	$(H/E_a)_{\text{crit}}$	H (W)	$p_{1,a}$ (kPa)	$10^3 U_{1,a}$ (m ³ /s)	phase $U_{1,a}$ (deg)	Γ
76	0.25	0.119	15.7	145	2.45	42.1	0.29
75	0.25	0.109	17.4	155	2.65	38.9	0.32
75	0.25	0.103	20.3	171	3.10	41.8	0.36
151	0.50	0.077	9.6	174	2.00	44.3	0.24
171	0.57	0.069	7.6	171	1.78	43.6	0.21
188	0.62	0.056	7.7	192	1.84	39.0	0.22
189	0.63	0.059	7.2	186	1.76	42.4	0.21
224	0.74	0.049	4.2	168	1.31	38.8	0.15
276	0.90	0.026	4.1	233	1.71	37.5	0.19

FIG. 1: Schematic drawing of an internal streaming flow in a regenerator. The x axis is the acoustic direction, and the y axis is the long transverse dimension. The extent of the regenerator along the z axis (not shown) is assumed to be small enough so that the acoustic and streaming flows are uniform in that direction. The arrows represent steady streaming flows induced by a small left-right temperature difference.

FIG. 2: Scale drawing of the orifice pulse tube refrigerator used in this study. All components from the aftercooler to the ambient manifold are annular. The rest of the components are circular. The four adapter tubes transition the annular geometry back to circular.

FIG. 3: Acoustic power leaving the piston face, E_p , versus the power dissipated in the variable acoustic load, E_{load} , for several different $|p_{1,a}/p_m|$. The lines are least squares fits to the data. The slopes of the lines range from 1.0 to 1.05, demonstrating the accuracy of determining E_p from $p_{1,a}$ and LVDT measurements of the piston location. The E_p intercept at each value of $|p_{1,a}/p_m|$ determines the acoustic dissipation due to boundary-layer processes in the experimental offset and piston seal leakage.

FIG. 4: Acoustic power dissipated by boundary-layer processes in the experimental offset and by piston seal leakage versus $|p_{1,a}/p_m|$. The fit to the data is used to interpolate between the data points.

FIG. 5: Measured and calculated acoustic pressure and volumetric velocity phasors throughout the experimental system at $|p_{1,a}/p_m| = 0.07$ and $T_c = 77$ K .

FIG. 6: Normalized measured temperatures around the azimuth at the axial midpoint of the regenerator for various $|p_{1,a}/p_m|$ and $T_c = 77$ K. See the text for how the temperatures have been normalized. The appearance of a sinewave-like distribution at higher $|p_{1,a}/p_m|$ signals the onset of an acoustic streaming instability.

FIG. 7: The amplitude squared of the Fourier transform of the temperature data in Fig. 6. The line is a least squares fit to the last three data points. The $|A|^2 = 0$ intercept is defined to be the onset of the instability, i.e. $(H/E_a)_{\text{crit}}$.

FIG. 8: $(H/E_a)_{\text{crit}}$ versus τ . Each point is an experimental value obtained from a data set like that of Fig. 7. The thin and bold lines are Eq. (52) with and without the transverse conduction term, respectively. To check the repeatability of the measurements, the group of three points near $\tau = 0.25$ were taken under nearly identical acoustic conditions, as was the pair of points near $\tau = 0.60$. The primary sources of uncertainty in $(H/E_a)_{\text{crit}}$ are the scatter in the individual temperature measurements used to determine $|A|^2$ and the choice of how many points in the plots of $|A|^2$ vs E_a/H to include in the linear fit (see Fig. 7).

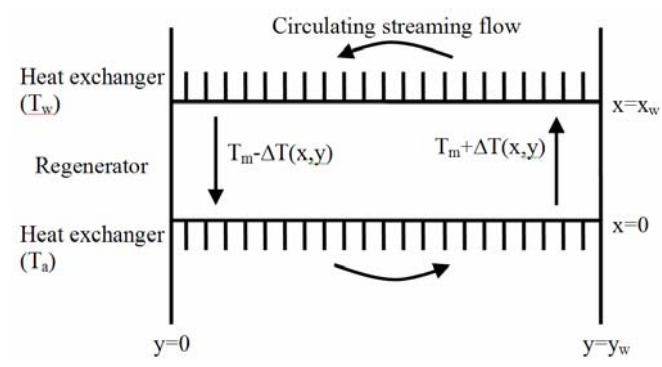


Figure 1: (So)

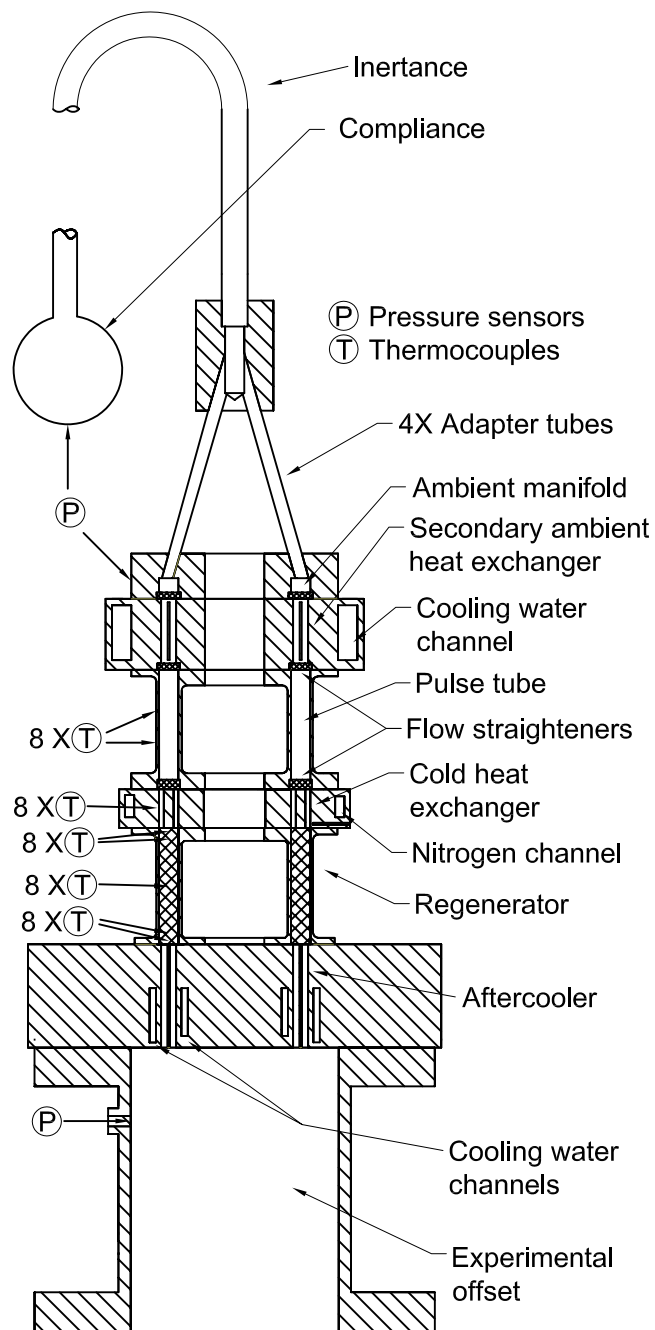


Figure 2: So

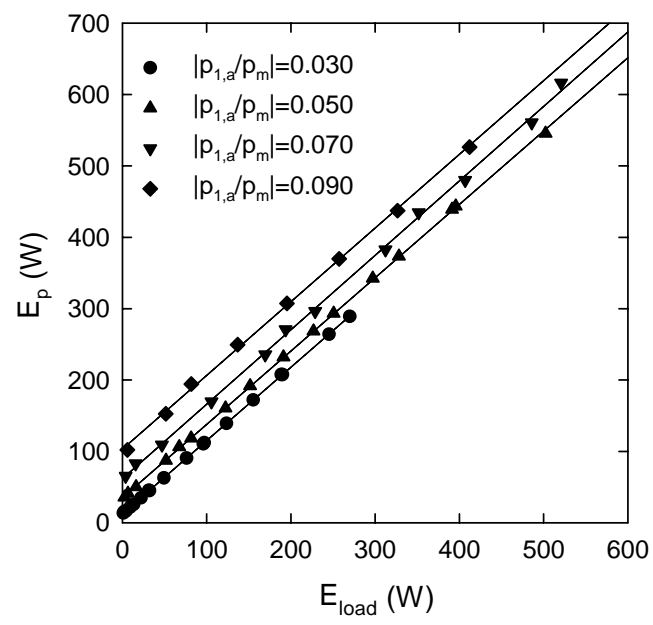


Fig. 3 (So)

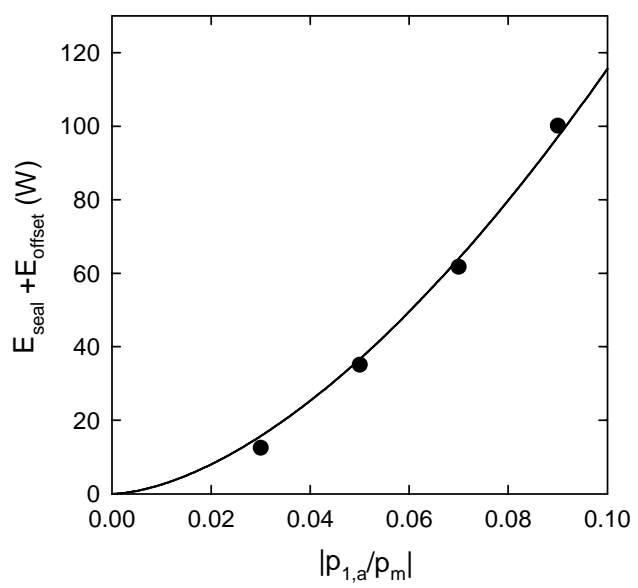


Fig. 4 (So)

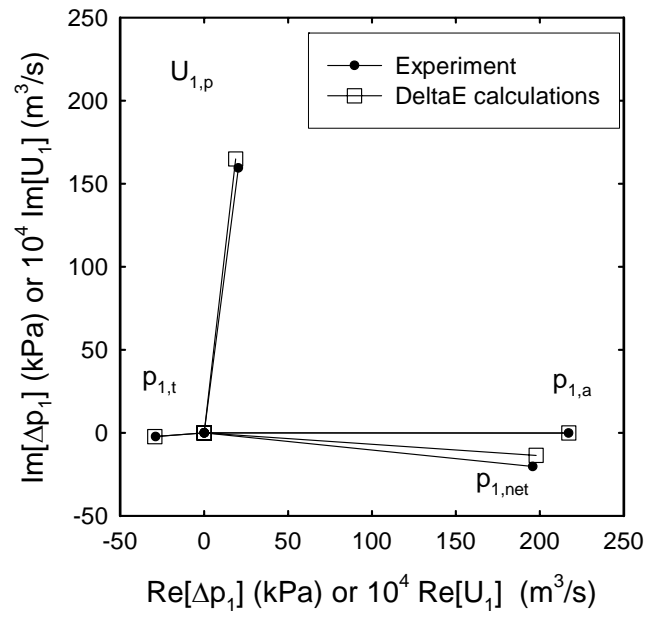


Fig. 5 (So)

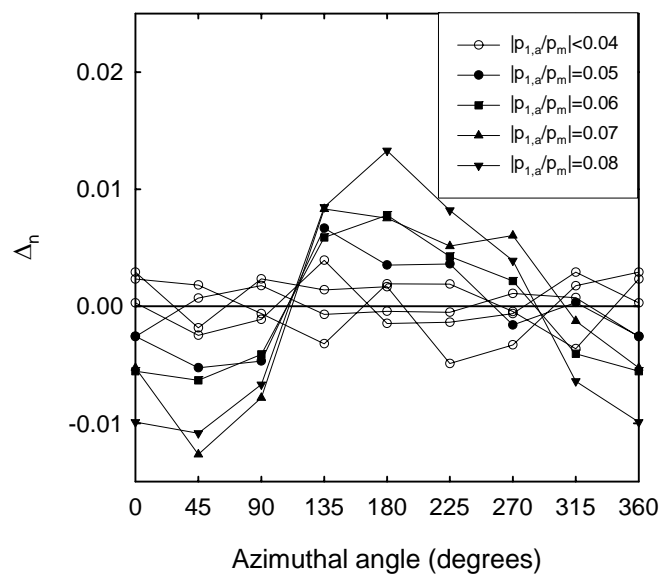


Figure 6 (So)

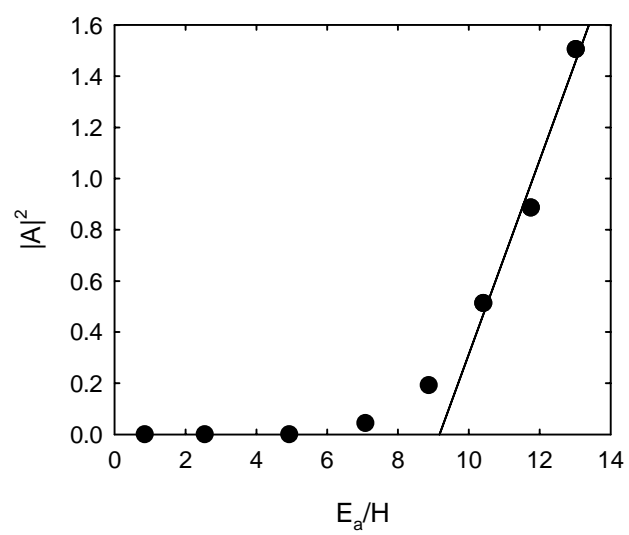


Fig 7 (So)

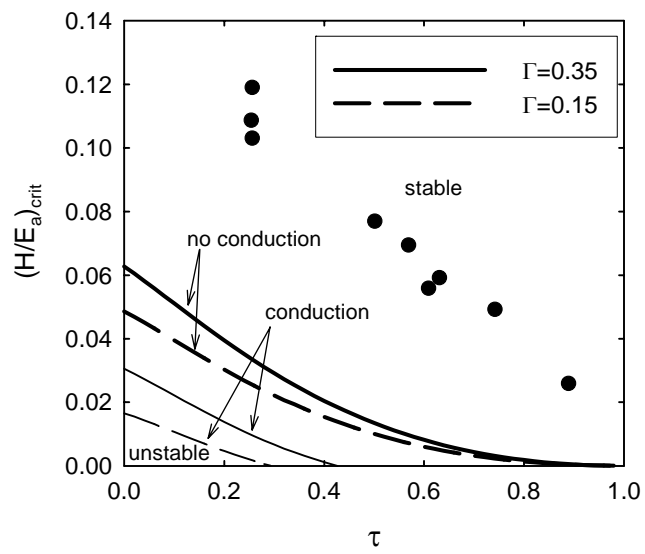


Figure 8 (So)